

# Cyclops: A Nanomaterial-based, Battery-Free Intraocular Pressure (IOP) Monitoring System inside Contact Lens

*paperID:231*

## Abstract

Intraocular pressure (IOP), commonly known as eye pressure, is a critical physiological parameter related to health. Contact lens-based IOP sensing has garnered significant attention in research. Existing research has been focusing on developing the sensor itself, so the techniques used to read sensing data only support a reading range of several centimeters, becoming the main obstacle for real-world deployment. This paper presents Cyclops, the first battery-free IOP sensing system integrated into a contact lens, which overcomes the proximity constraints of traditional reading methods. Cyclops features a three-layer antenna comprising two metallic layers and a nanomaterial-based sensing layer in between. This innovative antenna serves a dual purpose, functioning as both a pressure sensor and a communication antenna simultaneously. The antenna is connected to an RFID chip, which utilizes a low-power self-tuning circuit to achieve high-precision pressure sensing, akin to a 9-bit ADC. Extensive experimental results demonstrate that Cyclops supports communication at meter-level distances, and its IOP measurement accuracy surpasses that of commercial portable IOP measurement devices.

## 1 Introduction

Intraocular pressure (IOP) is a critical human vital sign of human health, and thus monitoring IOP is crucial for assessing and managing various diseases, especially glaucoma, the second leading cause of irreversible blindness worldwide [1–4]. Elevated IOP causes permanent damage to the optic nerve inside eyes, ultimately resulting in glaucoma and gradual vision loss. Glaucoma has no cure yet but if we detect Glaucoma in its early stage, we could prevent it from causing permanent vision by lowering the IOP via medicine or surgery. We emphasize that early-stage Glaucoma has no obvious symptoms, making accurate IOP measurement the only feasible solution for timely diagnosis of early-stage Glaucoma.

Furthermore, continuous and long-term tracking of IOP is necessary for accurate disease diagnosis and effective disease

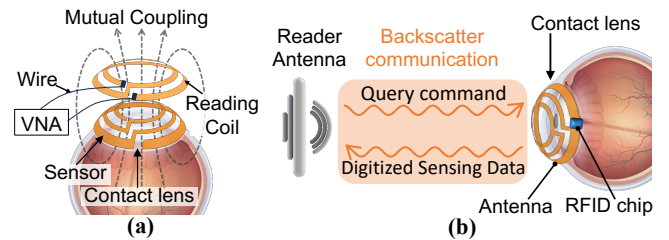


**Figure 1.** Reading data from contact lens via mutual coupling only supports centimeter level reading range (a), while backscatter based communication extends it to meter level(b).

management, since IOP naturally fluctuates in response to various physiological and psychological factors [5, 6], such as sleeping or dramatic emotional fluctuations. Accumulating long-term monitoring data helps eliminate the influence of unrelated factors, enabling accurate diagnosis. Additionally, timely tracking of IOP variations allows for precise and timely interventions, such as initiating medication immediately upon detecting elevated IOP to control the progress of Glaucoma.

Due to the significant impact of IOP on human health, accurate measurement has attracted a large amount of attention, particularly in biomedical engineering. Contact lens-based wearable techniques have emerged as the leading solution because of their lightweight nature, potential for mobility, and high accuracy resulting from direct contact with the eye balls. Two types of pressure sensors that fit in the contact lens have been the main focus of prior works: the piezoresistive sensors [4, 7–15], and the inductively coupled structure based sensors [16–24]. These sensors incorporate a ring structure made of conductive material that conforms to the shape of the contact lens, as depicted in Figure 1. In piezoresistive sensors, the ring structure's resistance is carefully designed to be pressure sensitive, while in coupled structure based sensors, the reactance is pressure sensitive. As a result, pressure can be inferred by measuring the impedance of both sensor types.

Optimizing the sensor to make it more sensitive, biosafe, transparent, and easy to manufacture has been the main focus, so in most current solutions, the contact lens only contains

pressure sensors. To read the sensing data from the sensors embedded inside the contact lens, a reading coil connected to a vector network analyzer (VNA) is positioned atop the sensors to measure the impedance, just as shown in Figure 1(a). However, this method only supports a very limited data reading range of a few centimeters. Our survey of 20 related works reveals that the maximum reading range reaches only **five centimeters**. Putting a bulky reader in close proximity to eye balls poses a significant hindrance to practicality and emerges as the primary obstacle for real-world deployment.

This paper presents, **Cyclops**, a battery-free contact lens based IOP sensing system that supports long-range data reading, eliminating the requirement for a bulky data reader to be in close proximity to the user. We achieve long-range communication by integrating a backscatter communication system with the pressure sensor, all within the small contact lens. A backscatter communication system requires a sizable metallic antenna. The current pressure sensor features a conductive ring structure. Embedding both the antenna and the ring structure in the contact lens with limited size and a thickness below  $200 \mu\text{m}$  results in mutual coupling and thus interference, impacting both communication and sensing performance.

Instead of directly integrating a backscatter antenna and an existing pressure sensor together, we introduce a novel approach: a dual-purpose antenna that serves as a pressure sensor and a communication antenna concurrently. Our design involves a three-layer sandwich-like antenna structure comprising two *metallic antenna layers* and a central *sensing layer*. The sensing capability arises from the nanomaterial utilized in the middle layer, which exhibits significant variations in intrinsic properties such as *conductivity* and *permittivity* in response to pressure changes. Simultaneously, the sensing layer, integrated into the antenna assembly, influences the overall impedance of the complete three-layer structure, rendering the entire system sensitive to applied pressure and effectively functioning as a pressure sensor. Additionally, through meticulous optimization of the two metallic layers' structure, we can align the antenna's impedance with that of the backscatter chip, enabling long-range communication.

To design a sensing layer that works robustly on a battery-free, purely energy-harvesting powered system, we have the following design goals:

- *Ultra-Low Power Consumption.* Our sensing layer's power consumption must be maintained at an absolute minimum to align harmoniously with the overall power profile of the integrated system.
- *Superior Sensitivity.* The ability of the sensing layer to detect subtle changes in IOP is utmost significance, necessitating an exceptionally high sensitivity level.
- *Thickness, Curvature and Transparency.* The sensing layer's dimensions, including thickness and curvature, must seamlessly match the contact lens. The sensing layer should be transparent to minimize interference to human view.

- *Biocompatibility and Biosafety.* The sensor must exhibit a rigorous level of biocompatibility.

To meet the design goals, we leverage a nanocomposite to fabricate our sensing layer. The nanocomposite consists of *hollow carbon spheres* (HCS) nanoparticles blended in the *polydimethylsiloxane* (PDMS)—the most widely used material for fabricating contact lens. Specifically, we fabricate a flexible HCS-PDMS sensing film with a thickness of tens of micrometers. This nanocomposite's flexibility enables it to conform to the curvature of the contact lens. Moreover, all the materials utilized, including HCS and PDMS, have already demonstrated their biocompatibility.

The two metallic antenna layers create an electric field across the HCS-PDMS sensing film, inducing the quantum tunneling effect between the HCS nanoparticles, resulting in a tunneling current. Pressure affects the film's thickness, changing the nanometer-level spacing between HCS, which, in turn, influences the strength of the tunneling current. The variations in tunneling current effectively change the conductivity of the sensing film, which consequently affects the permittivity of the nanomaterial [25]. We further enhance our HCS-PDMS sensing film's sensitivity to pressure through three optimizations: replacing normal UHCS with Urchin-like HCS (UHCS) for enhanced tunneling current, fine-tuning UHCS density to strike a balance between sensitivity and transparency, and adding microstructures to the surface of UHCS-PDMS sensing film to further boost the sensitivity.

Our dual-purpose three-layer antenna is connected to an RFID chip for backscatter communication. Matching the impedance of the antenna with that of the chip is crucial to maximize communication efficiency. It is, however, challenging to match the chip's impedance with our three-layer antenna whose impedance varies with the applied pressure. To tackle this problem, we propose to make the chip's impedance variable as well, allowing for dynamic real-time matching. We leverage the commercial Magnus S3 RFID chip that has a *self-tuning circuit* to adjust the chip impedance by modifying a 9-bit register. However, the self-tuning circuit has a limited range of *impedance tunability*. To ensure consistent matching, we have optimized the structure of the two metallic antenna layers to align the antenna's impedance tunability with the range of impedance variations induced by pressure, ensuring long-range communication.

To achieve high-resolution IOP sensing, precise measurement of the impedance variations in the three-layer antenna is essential. Traditionally, various methods have been employed to measure antenna impedance variations by analyzing the backscattered signal, such as tracking phase variations to infer impedance changes [26, 27]. It's worth noting that these methods are susceptible to channel dynamics and become ineffective when the human that wears the contact lens moves.

To mitigate the impact of human motion, we choose a different path: directly sampling and digitizing the impedance of the antenna within the RFID chip. However, this requires a

high-resolution analog-to-digital converter (ADC). To tackle this problem, instead of directly measuring the antenna's impedance, we opt to measure the impedance of the chip itself, which can be obtained from the 9-bit register of the self-tuning circuit. Consequently, this 9-bit register effectively serves as a 9-bit ADC, enabling high-resolution sampling and digitization. After data digitization, the reader then directly queries the Cyclops lens to fetch the digitized impedance.

We have developed cost-effective methods to fabricate the UHCS nanoparticles, the UHCS-PDMS nanocomposite sensing film, the three-layer antenna, and the Cyclops-lens. A substantial number of Cyclops lenses have been manufactured, and their IOP measurement performance has been tested in various environments. Extensive experimental results demonstrate that Cyclops achieves a communication distance of 1 meter, significantly surpassing the centimeter-level range of existing solutions. The IOP accuracy, when tested on artificial eyes and real pig eyes, achieves a median accuracy of 0.51 mmHg and 0.5 mmHg, respectively, surpassing that of commercial portable IOP measurement devices. We have also investigated the impact of tears and eyelids. Results show that Cyclops works robustly, achieving median accuracy of 0.55 mmHg, 0.54 mmHg, and 0.6 mmHg, with tears, eyelids, and both of them, respectively.

## 2 Related Work

**IOP Tonometry.** Clinical IOP measurement relies on various techniques, including Goldmann applanation tonometry [28], Dynamic contour tonometry [29], Tonopen tonometry [30], and Pneumatonometer [31]. However, these technologies lack the capability of continuous sensing and require trained medical personnel for operation. Implantable IOP biosensors [32–35] inside the anterior chamber, are the most accurate but also probably the most invasive techniques for IOP measurement.

**Contact-lens Based IOP Sensor.** Contact-lens based techniques are the dominant solution for the wearable IOP sensing design. Diverse types of pressure sensors that fit in the contact lens have been proposed. Piezoresistive sensors [4, 7–15] are one type of sensor whose resistance changes in response to the applied pressure. The main focus of research in this direction has been designing diverse conductive material whose resistance is sensitive to applied pressure. Some examples of the material are Ag nanowires (AgNWs) [36], gold hollow nanowires(AuHNW) [8], and Graphene-AgNWs [18]. Inductively coupled sensors [16–24], are sensors whose reactance changes with the applied pressure, so finding the structure whose capacitance or inductance is sensitive to pressure has been the main focus of research in this direction. The dominant data reading technique for both piezoresistive sensors and inductively coupled sensors are the mutual coupling based method as shown in Figure 1(a), which only supports a reading range of several centimeters. Microfluidic sensor [37–42]

is a special type of sensing technique that integrates microfluidic channels inside the contact lens. The pressure affects the distribution of liquid inside those microfluidic. However, observing the distribution of liquid requires a high-end camera placed in proximity of the contact lens and many other complicated, bulky, and costly optic infrastructures.

**Contact-lens Based Sensing Systems.** Besides measuring eye pressure, contact lens based devices are also used for blood glucose monitoring [43–45], integrated pixel display functions [46–50], and drug delivery [51–54]. The well-known contact lens system Google contact lens [43] utilize sensors to measure blood glucose levels through tears. Two commercial contact lens systems MoJo [46] and InWith [47] support displaying information on the contact lens. All of the three contact lens system require on-lens batteries. A recent work [51] design a contact lens capable of detecting glucose levels in tears, and drugs can be released from the self-regulated pulsatile drug delivery system through remote communication. Another work [48] develops a contact lens equipped with the capability to continuously monitor glucose levels in tears. This contact lens allows for tracking of diabetic conditions through and LED pixel display. Although these studies develop the new functionalities on contact lens, most works typically rely on on-lens batteries for power. Cyclops is a battery-free system that utilizes a commercial ThingMagic RFID reader to access the measurement data.

## 3 Nanomaterial-based Pressure Sensor

Our design of a pressure sensor with low power consumption and high sensitivity is rooted in the quantum tunneling effect occurring between nanoparticles. We expound upon this concept and present our design in the forthcoming sections.

### 3.1 Primer of Nanoparticles

In this section, we introduce the background of nanoparticles and the quantum tunneling effect between nanoparticles.

**Nanoparticles: Hallow Carbon Sphere.** We use hollow carbon sphere (HCS) in our system, which are spherical assemblies composed of carbon atoms, uniformly dispersed across the surface to encase an empty interior, as illustrated in Figure 2(a). These structures boast diameters in the range of hundreds of nanometers, with sphere thicknesses measured around 10 nm. This unique architecture imparts exceptional attributes to HCS, including robust electrical conductivity, chemical stability, thermal resilience, and mechanical durability. Furthermore, HCS exhibits great biocompatibility and biosafety [55], making it suitable for bio-related applications.

**Quantum Tunneling Effect.** We leverage a *quantum tunnel junction* to illustrate the phenomenon of quantum tunneling. A typical tunnel junction consists of two electrically conducting layers separated by a thin insulating layer, as depicted in Figure 2(b). Ordinarily, electrons within each conductive

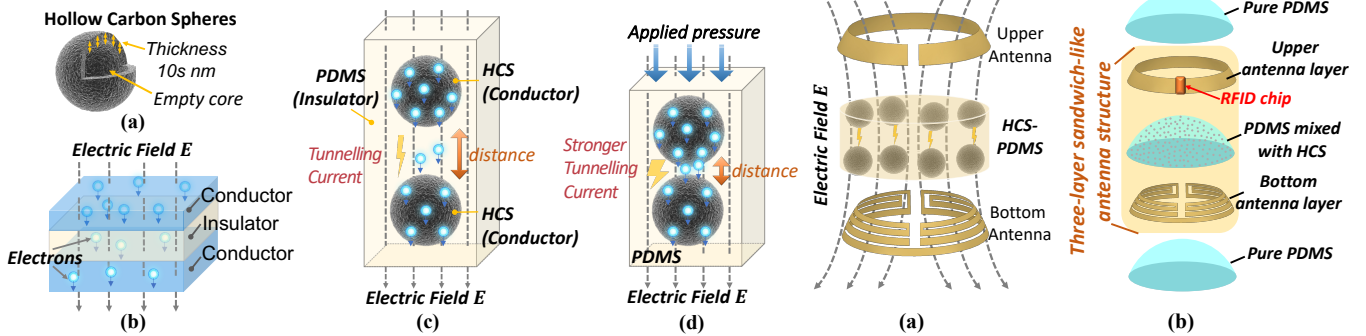


**Figure 2.** The model of the hollow carbon spheres is shown in (a). The model of the tunnelling junction is shown in (b). The quantum tunneling effect between hollow carbon spheres is depicted in (c). Applied imposition of pressure on the construct is illustrated in (d).

layer are unable to traverse the insulating layer and access the adjacent conductive layer. However, the introduction of an external electric field helps electrons overcome this barrier, thereby giving rise to a *quantum tunneling current*. As per quantum theory, the magnitude of this tunneling current hinges on two primary factors: the thickness of the insulating layer and the intensity of the applied electric field.

**Quantum Tunneling Effect between HCS.** Resembling the tunnel junction, when we embed two electrically conductive HCS inside any insulating material and apply an external electric field, we will observe quantum tunneling current between two HCS particles, just as shown in Figure 2(c). The magnitude of the tunneling current depends on the distance between HCS particles and the intensity of the applied electric field.

### 3.2 Naonomaterial-based Pressure Sensing

We introduce the design of our nanomaterial-based pressure sensor that leverages the quantum tunneling effect.

#### 3.2.1 Sensing Structure and Sensing Mechanism.

Adhering to the tunneling junction structure, we embed HCS that function as conductors inside the *polydimethylsiloxane* (PDMS), which serves as the insulator, as depicted in Figure 2(c). This configuration yields what we term an HCS-PDMS nanocomposite material. Notably, we select PDMS as it is the most widely employed material for manufacturing contact lenses, being both an efficient insulator and showcasing remarkable biocompatibility and biosafety characteristics.

Application of an external electric field to the HCS-PDMS initiates the emergence of a quantum tunneling current between adjacent HCSs, akin to the portrayal in Figure 2(c). Upon the imposition of pressure on the HCS-PDMS construct, the entire layer undergoes thinning, leading to a proportional reduction in the spacing between the HCSs. As elaborated in previous sections, a decrease in the gap between the conductors amplifies the potency of the quantum tunneling effect,

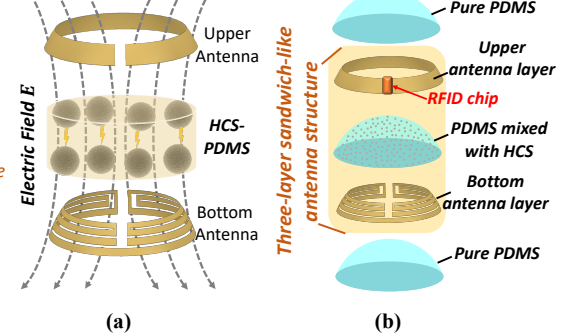


**Figure 3.** Two metallic antenna layers with different structures are used to power the pressure sensor as illustrated in (a). The complete five-layer contact lens antenna structure is shown in (b).

ultimately giving rise to an escalated tunneling current. Consequently, pressure can be measured by assessing the intensity of the resultant tunneling current.

#### 3.2.2 Powering the Pressure Sensor

The proper functioning of our pressure sensor relies on the presence of an external electric field. Conventionally, the predominant method for generating an electric field involves employing electrodes connected to a power source. This potential difference between the electrodes establishes the electric field. However, our contact lens operates without a traditional power source, being driven solely by energy-harvesting mechanisms. As a result, creating such an electric field within a battery-free device poses a significant challenge.

**Three-layer Sandwich-like Antenna Structure.** In order to energize the sensor on our battery-free device, we introduce a 3-layer sandwich-like antenna structure. This configuration involves two distinct metallic antenna layers, flanking a central HCS-PDMS film (*i.e.*, the pressure sensor) as depicted in Figure 3(a). Notably, the two metallic antenna layers are designed to have different structures. Consequently, when the interrogation signal from the reader interacts with the tag, distinct surface currents are induced on the two antenna layers, resulting in disparate current distributions. This, in turn, naturally engenders a potential difference and establishes an electric field between the two antenna layers. This process successfully applies an external electric field to the HCS-PDMS film, thus powering the sensor.

**Complete Five-layer Contact Lens Design.** Direct interaction between the metallic antennas and human tissue is considered biologically unsafe. In response, we encapsulate both the sensor and the tag antenna with two additional layers of biosafe PDMS. Following this enhancement, a 5-layer contact lens configuration is achieved, as depicted in Figure 3(b). Among those layers, the two pure PDMS layers and two metallic antenna layers have a thickness of 30  $\mu\text{m}$  and 10  $\mu\text{m}$ , respectively. The thickness of the HCS-PDMS

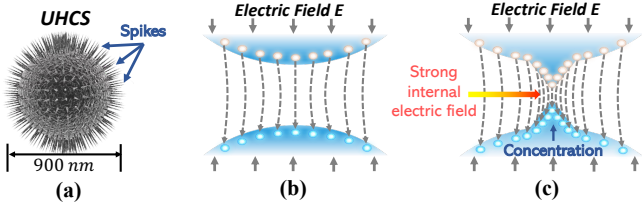


**Figure 4.** The urchin-like HCS (UHCS) has uniformly distributed spikes on its surface, creating a much stronger internal electric field compared to HCS without spikes.

sensing film is  $60 \mu\text{m}$ . Consequently, the overall thickness of the complete contact lens amounts to  $140 \mu\text{m}$ .

### 3.2.3 Maximizing the Sensitivity.

We have made three optimizations to our nanomaterial-based pressure sensor to maximize its sensitivity.

**Urchin-like HCS.** To generate a stronger tunneling current under the same external electric field, we make a structural modification to the carbon sphere. Specifically, we replace the normal HCS with urchin-like hollow carbon sphere (UHCS) whose structure is depicted in Figure 4(a). The surface of the urchin-like carbon sphere features long, sharp, and uniformly distributed spikes. When subjected to an external electric field, a substantial concentration of free electrons accumulates on these spikes, engendering a markedly intensified internal electric field in contrast to the smooth-surfaced normal HCS, as shown in Figure 4(b) and (c). This augmented internal electric field significantly facilitates electron traversal across the insulating space between the carbon spheres, resulting in an amplified tunneling current. Moreover, the presence of spikes on the carbon sphere serves to diminish the gap between neighboring carbon spheres, particularly at low filling concentrations, thereby further augmenting the tunneling current.

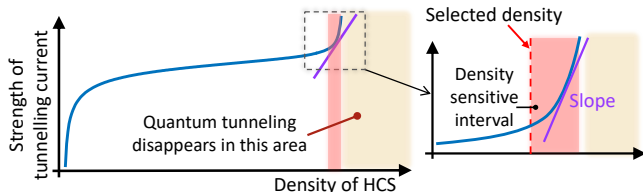


**Figure 5.** The relationship between the strength of tunneling current and the density of UHCS inside of the PDMS.

**Optimizing the UHCS Density.** The distance between the carbon spheres, which corresponds to the density or concentration of carbon spheres within the PDMS, holds notable influence over the resultant tunneling current. We have constructed a model and subsequently conducted simulations to discern the connection between the intensity of the quantum tunneling current and the density of UHCS. The simulated outcomes, graphically presented in Figure 5, yield two key observations. Firstly, the quantum tunneling phenomenon disappears when

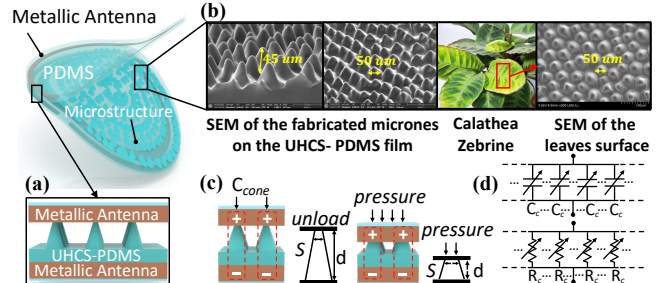


**Figure 6.** The microstructure of the UHCS-PDMS film is depicted in (a). The scanning electron microscopy (SEM) imaged microstructure is illustrated in (b). The schematic of the pressure sensing is illustrated in (c). Circuit schematic diagram of pressure sensing is depicted in (d).

the distance between carbon spheres decreases too much (density surpassing  $2.06 \text{ wt.\%}$ ). Secondly, a density-sensitive interval (ranging from  $1.72 \text{ wt.\%}$  to  $2.06 \text{ wt.\%}$ ) emerges, within which even minor fluctuations in density yield substantial variations in the generated tunneling current's strength.

To optimize sensitivity, we configure the density of UHCS at the start of this density-sensitive interval, just as illustrated in Figure 5. This strategic selection ensures that minute fluctuations in pressure yield significant deviations in the magnitude of the resulted tunneling current.

**Bio-inspired Microstructures.** To further improve the sensitivity, we introduce microstructures of the UHCS-PDMS sensing film. Specifically, we create a large number of *microcones* on the surface of the sensing film, each with an average diameter of  $50 \mu\text{m}$  and height of  $45 \mu\text{m}$ , just as shown in Figure 6. The apex of each microcone connects to the antenna layer, while the base of the cone interfaces with the surface of the sensing film, as depicted in Figure 6(a). For the purpose of structural stability, the residual space between the antenna and the microcones is filled with pure PDMS.

Each microcone serves as a connection point between two antenna layers, effectively functioning as a resistor. The resistance  $R_c$  of such a resistor is given as:

$$R_c = \frac{1}{\sigma S} \quad (1)$$

where  $\sigma$  represents the conductivity of the material, namely the UHCS-PDMS nanocomposite and  $S$  denotes the *area of the plate*, which is the contact area between the cone and the upper antenna layer. As per our empirical observations outlined in §6.1, an increase in applied pressure not only expands the contact area  $S$ , but also increases the conductivity of the material, primarily due to a more pronounced tunneling effect, consequently resulting in decreased resistance  $R_c$ .

The combination of the two metallic antenna layers and the cone in between also forms a parallel plate capacitor, as shown in Figure 6(c), whose capacitance  $C_{cone}$  is:

$$C_{cone} = \frac{\epsilon S}{4\pi d} \quad (2)$$

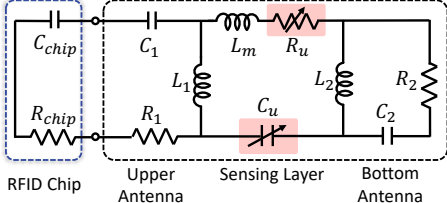


**Figure 7.** The equivalent circuit of the Cyclops lens antenna, where  $C_u$  and  $R_u$  represents a variable capacitor and resistor.

where  $\epsilon$  represents the *permittivity* of the UHCS-PDMS nanocomposite, and  $d$  is the distance between two plates, *i.e.*, two antenna layers. When pressure is applied, the entire three-layer antenna gets thinner, leading to an expansion in the contact area  $S$  between the cone and the antenna and a reduction in the distance  $d$  between the two antenna layers. As per our empirical findings in §6.1, this process also results in increased permittivity  $\epsilon$  of the nanocomposite. Consequently, an increase in pressure leads to a corresponding increase in capacitance  $C_c$  of each microcone-antenna capacitor.

In summary, the incorporation of microcone introduces an array of pressure-sensitive capacitors and resistors connected in parallel, just as shown in Figure 6(d). Consequently, the overall impedance of the entire sandwich-like structure becomes responsive to pressure, whose resistance can be represented as:

$$R_u = \frac{1}{\sum_{k=1}^K \frac{1}{R_{c_k}}} \quad (3)$$

and capacitance is given as:

$$C_u = \sum_{k=1}^K C_{c_k} \quad (4)$$

assuming there are  $K$  microcones added to the film.

*Fabrication of microcones.* The fabrication of a microcone structure demands advanced MEMS technology, involving costly equipment and skilled operators. In response, we propose a bio-inspired microcone fabrication technique that notably mitigates fabrication complexity and cost. Our approach stems from the observation that Calathea Zebrine [56] leaves possess a remarkably uniform microcone surface structure, as evidenced in Figure 6(b). Leveraging this natural inspiration, we propose to produce a microcone template utilizing Calathea Zebrine leaves<sup>1</sup>. Subsequently, we replicate the surface pattern from this microcone template onto the sensing film, effectively generating uniform microcone structures.

### 3.2.4 Integrated Sensing System

We connect an RFID chip to our three-layer antenna for backscatter communication, just as shown in Figure 3(b). The RFID chip we use is Magnus S3 [57] with a known and fixed chip impedance  $Z_{chip} = \text{Re}(3.99 \Omega) + \text{Im}(91.05 \Omega)\text{j}$ . The

<sup>1</sup>The detailed microcone template fabrication process using Calathea Zebrine leaf can be found in Appendix §A.1.

equivalent circuit diagram of our sensing system is shown in Figure 7. In such an integrated sensing and communication system, the three-layer antenna functions as both a pressure sensor and a communication antenna. The impedance of the three-layer antenna depends on two categories of factors:

- *Antenna-dependent static components.* All these components are fixed if the structures of those two metallic antenna layers are known. Specifically,  $C_1$  and  $C_2$  represent the *parasitic capacitance* associated with the two antenna layers;  $R_1$  and  $R_2$  denote the *parasitic resistance* of the respective antenna layers;  $L_1$  and  $L_2$  correspond to the *parasitic self-inductance* of two antenna layers;  $L_m$  is the *mutual-inductance* between two antenna layers.
- *Pressure-dependent variable components.* The impedance of the sandwich-like three-layer structure  $C_u$  and  $R_u$  varies when the applied pressure varies.

**Antenna Impedance.** Based on the equivalent circuit shown in Figure 7(b), we derive the overall impedance of the whole three-layer antenna as:

$$Z_{ant} = -\frac{1}{j\omega C_1} + R_1 + \frac{j\omega L_1(Z_s + Z_b)}{j\omega L_1 + Z_s + Z_b} \quad (5)$$

where  $Z_s$  and  $Z_b$  are:

$$Z_s = -\frac{1}{j\omega C_u} + R_u + j\omega L_m, \quad (6)$$

$$Z_b = \frac{\omega^2 R_2 L_2 C_2 + j\omega L_2}{1 + \omega^2 C_2 L_2 - j\omega R_2 C_2}. \quad (7)$$

The detailed process of deriving the antenna impedance is presented in Appendix B. According to Eqn. 5, we know that any variations in pressure change the value of the pressure-sensitive resistor  $R_u$  and capacitor  $C_u$ , which in turn affects  $Z_s$ , ultimately changing the impedance  $Z_{ant}$  of the entire three-layer antenna. Therefore, our three-layer antenna effectively functions as a pressure sensor whose impedance value is directly associated with the applied pressure.

## 4 Concurrent Sensing and Communication

In this section, we present our system design that integrates the dual three-layer and the RFID chip into one battery-free IOP sensing system that simultaneously achieves high sensing accuracy and supports long range communication.

### 4.1 Long-Range Backscatter Tag Design

To support long-range backscatter communication, it is imperative to match the impedance of the commercial RFID chip with the impedance of our three-layer antenna. Since the impedance of an antenna changes with the operating frequency, our objective is to design an antenna that matches its impedance  $Z_{ant}$  with the chip impedance  $Z_{chip}$  at its *operating frequency*  $f_c$ , *i.e.*,  $Z_{chip} = Z_{ant}(f_c)$  just as shown in Figure 8(a). It is essential to emphasize that the operating frequency  $f_c$

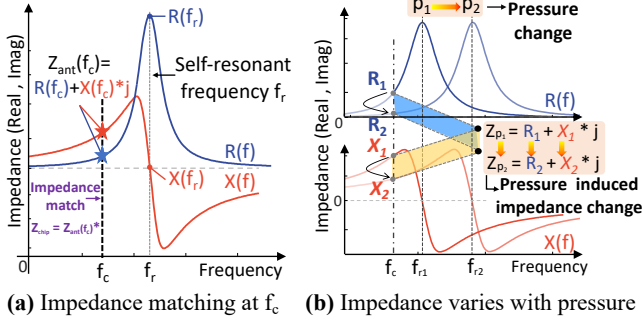


**Figure 8.** The antenna impedance fluctuates with both frequency and applied pressure. We focus on achieving impedance matching at the operating frequency.

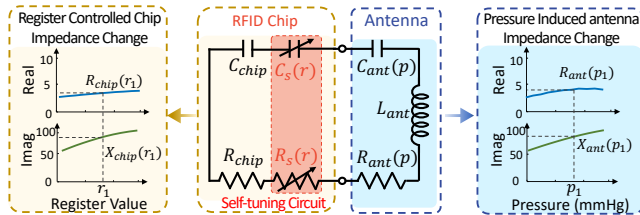


**Figure 9.** The equivalent circuit of the Cyclops with the self-tuning circuit, where  $C_s$  and  $R_s$  represents a variable capacitor and resistor values that vary based on the register value.

of our system differs from the *self-resonant frequency*<sup>2</sup>  $f_r$  of the antenna because our chip has close-to-zero resistance ( $R_c=3.99 \Omega$ ) and high reactance ( $X_c=91.05 \Omega$ ).

**Challenge: Antenna Impedance Fluctuations.** When the applied pressure changes, the antenna impedance distribution across frequencies  $Z_{\text{ant}}(f)$  changes accordingly, as depicted in Figure 8(b). In contrast, the chip impedance  $Z_{\text{chip}}$  is pressure-oblivious and thus remains constant. As a result, the impedance of the antenna and the chip cannot maintain matching as applied pressures fluctuate, which could significantly impact the communication efficiency of our system.

**Solution: Self-tuning Circuit.** We leverage the self-tuning circuit inside the commercial Magnus S3 RFID chip to dynamically adjust the impedance of the chip to match the variable antenna impedance, just as shown in Figure 9. The self-tuning circuit effectively functions as a variable capacitor  $C_s(r)$  and resistor  $R_s(r)$ , with  $r$  representing the value of a 9-bit self-tuning register. The RFID chip fine-tunes its impedance by adjusting the self-tuning register's value, making the chip impedance also variable, denoted as  $Z_{\text{ant}}(r)$ .

Each time the chip powers on, it initiates a search for the optimal  $r_m$  value that achieves impedance matching with the connected antenna. The key insight the chip leverages is that antenna efficiency is at its peak when impedance is well-matched. Consequently, the RFID chip attempts to discover

<sup>2</sup>Self-resonant frequency is defined as the frequency where the antenna resistance is maximized and at the same time reactance is zero.

the ideal  $r_m$  value that maximizes the RSSI of the received signal, as detailed in [57]. Once this optimal  $r_m$  is identified, the chip locks its register value to  $r_m$  to ensure continuous impedance matching between the chip and the antenna.

## 4.2 High-Resolution Pressure Sensing

To obtain precise digital pressure measurements, we need to accurately measure the impedance of the three-layer antenna and subsequently digitize the measured impedance using a high-resolution analog-to-digital converter (ADC). However, several challenges emerge. First, impedance measurement typically relies on a vector network analyzer, a sophisticated and costly equipment unsuitable for integration within a contact lens. Furthermore, even if the contact lens possessed adequate space for housing a high-resolution ADC, the energy constraints of a battery-free device present significant hurdles in powering such a component.

**Solution: Effective 9-bit ADC via Impedance Matching.** We rely on the real-time impedance matching scheme to achieve simultaneous antenna impedance measurement and digitization. The underlying concept hinges on the fact that the applied pressure, which can be denoted as  $p$ , governs the overall impedance of the three-layer antenna, which can be denoted as  $Z_{\text{ant}}(p)$ . In parallel, the RFID chip adjusts its register value  $r$ , thus modifying its own impedance  $Z_{\text{chip}}(r)$ , as illustrated in Figure 10(a). To maximize the communication efficiency, the chip searches for  $r_m$  that guarantees the state of the impedance matching between the chip and antenna:

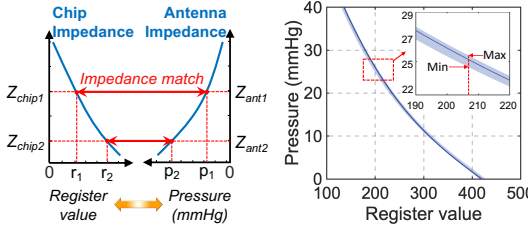
$$Z_{\text{ant}}(p) = Z_{\text{chip}}(r_m). \quad (8)$$

Eqn. 8 effectively establishes a mapping between the applied pressure  $p$  and the chip register value  $r_m$ . For instance, Figure 10(b) plots the relationship between the pressure  $p$  and register value  $r_M$  we collected from our fabricated contact lens, based on which, we can derive the applied pressure  $p$  from the chip register value  $r_m$  that achieves impedance matching. Moreover, the 9-bit chip register inherently functions as a 9-bit ADC that digitizes the sensing value, granting exceptionally high pressure-sensing resolution.

The chip stores the 9-bit register value at a specific location (from 0xC7 to 0xCF for Magnus S3) inside its memory bank. The reader sends a standard C1G2 command, *i.e.*, the *read* command that contains the exact location of the register inside the memory bank, to fetch the value  $r_m$  from the chip, based on which, the reader derives the pressure according to the pressure-register mapping in Figure 10(b).

## 4.3 Dual-Purpose Antenna Design

Our three-layer antenna serves a dual purpose, functioning as both a communication antenna and a pressure sensor with a sensing range spanning from 0 mmHg to 40 mmHg. To concurrently optimize communication and sensing perfor-



(a) Theoretic mapping.

(b) Mapping in practice.

**Figure 10.** The impedance matching naturally creates a mapping between the register value  $r_m$  and the applied pressure  $p$ .

mance, the antenna's impedance variations under various pressures within the sensing range should align with the chip's *impedance tunability*, *i.e.*, the range of impedance achievable by the chip via modifying the value of the 9-bit register. First, it is crucial to ensure that all potential antenna impedances fall within the tunability range of the chip. Any outlier leads to impedance mismatches, thereby adversely affecting communication efficiency. Furthermore, to make the most of the 9-bit ADC's resolution, the antenna's impedance variance range should occupy the chip's tunability to the greatest extent possible, as visually represented in Figure 11.

The Magnus S3 chip exhibits substantial tunability in reactance, ranging from  $59 \Omega$  to  $91 \Omega$ , while its resistance tunability is negligible, spanning from  $1 \Omega$  to  $4 \Omega$ . Hence, our antenna design should prioritize sensitivity to pressure-induced reactance variations while remaining less responsive to changes in resistance. Except for the requirement on the antenna impedance variance, our antenna design must meet two additional criteria. Firstly, it should be sized, shaped, and curved to seamlessly integrate with the contact lens. Secondly, the two metallic antenna layers must exhibit distinct structures to enable the generation of an electric field between them, thus powering the sensor, as illustrated in Figure 3(a).

**Dual Resonant Frequency Antenna Structure.** We leverage a dual resonant frequency antenna structure to effectively align the antenna impedance variations with the chip's tunability. Just as shown in Figure 12(a), we create two resonant frequencies  $f_{r1}$  and  $f_{r2}$  on both sides of the working frequency  $f_c$  through antenna structural design. We could see that, compared to the single resonant frequency antenna in Figure 8(a), the resistance variations near the operating frequency  $f_c$  exhibit a flat slope while the reactance variations have a sharp slope. As shown in Figure 8(b), the applied pressure induces a shift in the impedance distribution of one antenna across frequencies. Such a shift in impedance distribution for our dual-frequency antenna leads to substantial variations in reactance while keeping resistance changes to a minimum just as shown in Figure 12(b) and (c). Such a trend in impedance variations aligns with the chip's tunability.

We follow the steps depicted in Figure 13 to create such a dual-frequency antenna and confine its impedance variations

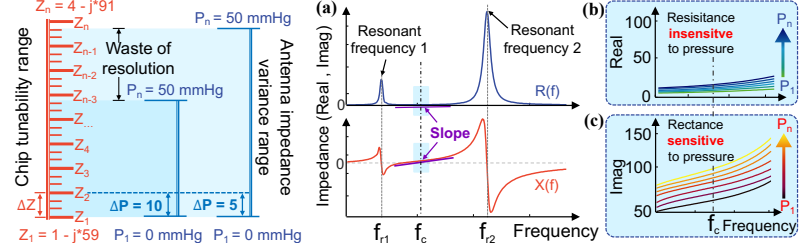


**Figure 11.** Aligning the **Figure 12**. A dual-frequency antenna results in significant pressure-induced reactance variations with chip's actions but minimal resistance variations at the operating frequency.

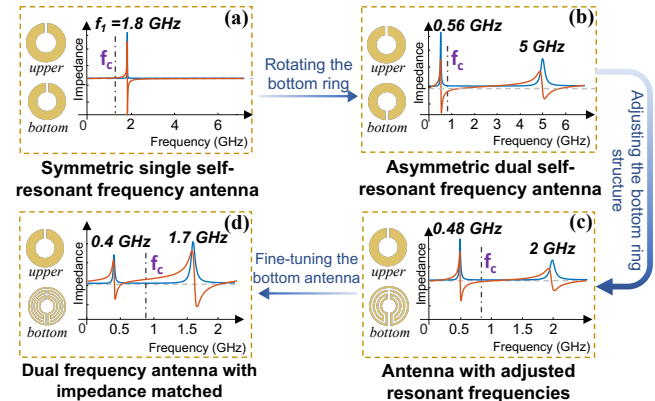
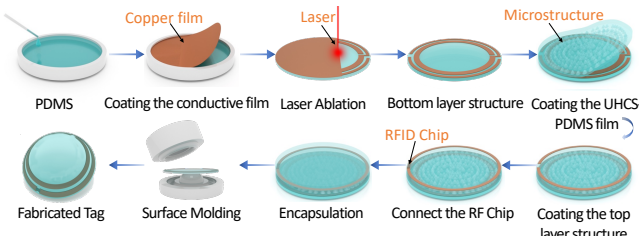
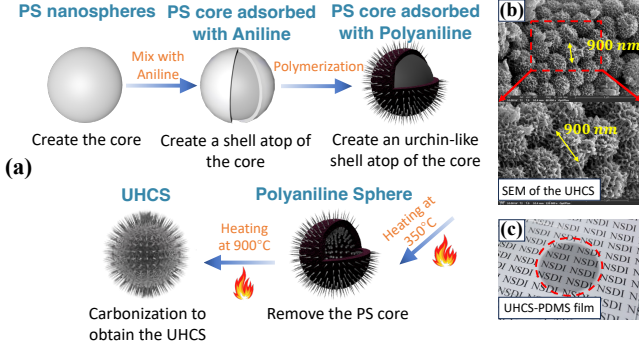


**Figure 13.** The workflow of creating a dual-frequency antenna structure and confining the antenna's impedance variations within the chip's tunability.

within the chip's tunability. Our three-layer antenna consists of two conductive layers separated by an intermediate dielectric layer. We initially start with a completely symmetrical antenna structure, just as shown in Figure 13(a), which exhibits only a single resonant frequency near the operating frequency (0-3 GHz). After experimenting with various methods to create a second resonant frequency on such a small antenna, we surprisingly find out that, the easiest way to break the symmetry is by rotating the bottom layer as shown in Figure 13(b). This asymmetry results in a significant shift in the original self-resonant frequency, moving it from 1.8 GHz to 0.5 GHz, while concurrently inducing the emergence of another self-resonant frequency at 5 GHz.

We also observe that increasing the electric length of the bottom layer significantly lowers the frequency of the second resonant frequency while keeping the first frequency less affected. Therefore, we gradually increased the length of the bottom layer antenna and shifted two resonant frequencies to 0.48 GHz and 2 GHz respectively, as shown in Figure 13(c). Finally, by making fine adjustments to the bottom layer's dimensions, such as the ring width and the gap between adjacent



rings<sup>3</sup>, we were able to finely tune the impedance distribution to ensure that pressure-induced variations remain within the chip's tunability as shown in Figure 13(d).

## 5 Implementation and Fabrication

**Synthesis of UHCS.** We employ the seeded swelling polymerization method [58] to synthesize *polystyrene* (PS) nanospheres. We then mix the fabricated PS nanospheres with *aniline* and add *iron(III) nitrate* to initiate the polymerization of aniline. This procedure results in the formation of an urchin-like *polyaniline* shell atop the PS nanospheres, as shown in Figure 14(a). After the washing and drying, we subject the spiky polyaniline to a temperature of 350°C within an *argon* atmosphere, effectively eliminating the PS core and leaving behind the shell structure. The final step involves subjecting the urchin-like polyaniline shell to a temperature of 900°C to initiate the carbonization of the shell, yielding the UHCS material. A detailed quantitative description of the synthesis process can be found in Appendix §A.2. Figure 14(b) depicts the scanning electron microscope (SEM) images of the fabricated UHCS whose mean sphere diameter is 900 nm.

**Fabrication of UHCS-PDMS with Microstructure.** We disperse the UHCS powder inside the PDMS solution with a mass fraction of 1.75 wt.%. Subsequently, we employ a spin

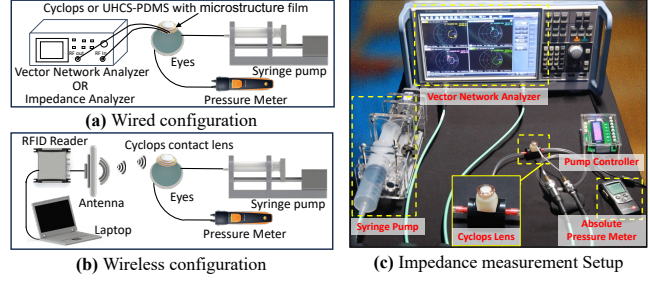


**Figure 16.** IOP measurement and material characteristic measurement platform for controlled experiments.

coating process to apply the blended solution onto the *Calathea Zebrina* template with microstructures. The solution and template are then heated at 80°C for an hour to produce the UHCS-PDMS film. A detailed UHCS-PDMS film fabrication process can be found in Appendix §A.3. Figure 14(c) shows a circular film of the UHCS-PDMS with a radius of 3 cm, showcasing exceptional transparency.

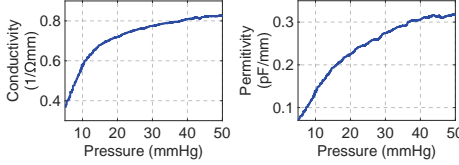
**Fabrication of Contact Lens.** Figure 15 details the workflow for crafting our contact lens. We start by shaping a copper film using laser engraving machine to match the proposed antenna structure and place it on a pure PDMS film. We then put the UHCS-PDMS film with microstructures atop the first antenna layer. Then, we etch the copper film using a laser engraving machine to create the upper layer antenna, which is connected directly to the RFID chip. We then place the upper layer antenna on the UHCS-PDMS film. To ensure bio-safety, we encase the upper layer antenna in an additional pure PDMS film. After a preliminary shaping step of subjecting it at 80°C for 10 minutes, we transfer the structure to a contact lens mold and thermally cure it at 80°C for one hour.

## 6 Evaluation

**Measurement Setup.** We fabricate a plastic prosthetic eye, which is a curved 3D eye model featuring an inlet connected to the syringe pump for precise pressure control and an outlet connected to a testo 510 pressure meter [59] to establish the accurate ground truth for applied pressure. We program the syringe pump controller to regulate the inflation speed and thus the applied pressure, as shown in Figure 16(c). We wirelessly collected real-time pressure from the pressure meter.

This platform serves as the basis for a variety of measurements. To assess the impedance, conductivity, or permittivity of materials or antennas, we position the fabricated sensing film or antenna atop the eyes and connect the material or antenna to an impedance analyzer (HIOKI IM7580 [60]) or a vector network analyzer (R&S ZNB8 [61]) using wire, just as shown in Figure 16(a) and (c). For evaluating the performance of the developed contact lens, we use a ThingMagic M6 reader [62] to query the chip, as shown in Figure 16(b).

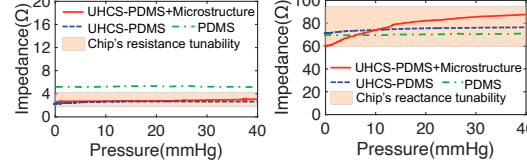
<sup>3</sup>The detailed antenna fine-tuning process is in Appendix C.



(a) Conductivity.

(b) Permittivity.

**Figure 17.** The properties of intermediate film under varying applied pressure.



(a) Resistance.

(b) Reactance.

**Figure 18.** The pressure-induced impedance variations of different materials.

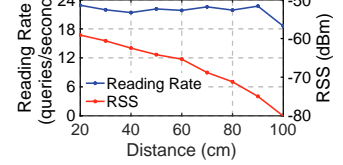


**Figure 19.** The measured RSS and reading rate at varying reader-chip distances.

## 6.1 Hardware Verification

**Verification of the Fabricated Nanocomposite.** To validate the characteristics of the nanocomposite, we place the UHCS-PDMS film, containing microstructures with a thickness of  $60\ \mu\text{m}$ , between two conductive copper films. We cut the dimensions of the film slightly larger than those of the copper layers to prevent short-circuiting between the upper and lower copper layers. Subsequently, we connect the copper films to an impedance analyzer and measure the conductivity and permittivity under varying pressure conditions. The results are presented in Figure 17, clearly demonstrating that applied pressure influences the conductivity and permittivity of the UHCS-PDMS film. Specifically, higher applied pressure corresponds to greater conductivity or permittivity, thus corroborating the theory outlined in §3.2.3.

**Validating the Alignment with Chip’s Tunability.** We conduct an investigation into the range of pressure-induced impedance variations in our three-layer antenna. Specifically, we connect the antenna to a vector network analyzer and apply varying levels of pressure. For comparison, we replace the pure PDMS film with UHCS-PDMS film without microstructures and UHCS-PDMS with microstructures. We maintain same thickness across all the three films. The measured impedance, along with the chip’s impedance tunability, is presented in Figure 18(a) and (b), yielding two notable observations. First, the impedance of both types of UHCS-PDMS film falls within the chip’s tunability range, while the resistance of the pure PDMS falls outside of this range. Second, the impedance variation range of the UHCS-PDMS with microstructures covers a significantly wider span of the chip’s reactance tunability, indicating higher sensitivity when compared with the pure UHCS-PDMS without microstructures.

**Communication Range.** In this section, we explore the communication range of our three-layer antenna. We employ our reader to interrogate the RFID chip embedded in the contact lens and record two key parameters: the received signal strength (RSS) and the reading rate, which represents the number of successful pressure queries per second. We conduct these measurements at various distances ranging from 20 cm to 1 m and present the findings in Figure 19. It is evident from the results that as the communication distance increases, the RSS decreases, eventually reaching  $-80\ \text{dBm}$  at a distance of 1 m. Similarly, the reading rate maintains

at  $22\ \text{queries}/\text{second}$  within the communication range and slightly decreases to  $19\ \text{queries}/\text{second}$  when approaching the 1-meter communication range. Beyond this boundary, a stable connection between the reader and the RFID chip becomes unattainable. To our knowledge, achieving a communication range of 1 m is a significant advancement compared to existing contact lens-based IOP measurement systems.

## 6.2 IOP Measurement Performance

We begin with an end-to-end experiment to gain an insight into how Cyclops works, followed by the verification of IOP measurement performance from various angles.

**End-to-end Performance.** We use the experimental setup illustrated in Figure 16 to control the applied pressure and also record the ground truth using pressure meter. We use the reader to query the tag for the register value and derive the pressure according to the mapping. We repeat the experiments at various locations, including an office ( $5\text{m} \times 7\text{m}$ ) with several tables, an activity room ( $10\text{m} \times 8\text{m}$ ) full of furniture, and a corridor ( $20\text{m} \times 8\text{m}$ ) with several billboard sets, as shown in Figure 20. At each location, we vary the chip-reader distance from 20 cm to 1 m with a step size of 10 cm.

We plot the CDF of the IOP measurement error in Figure 21, from which we see that the median error is around  $0.51\ \text{mmHg}$  and the  $70\%$  error is around  $0.8\ \text{mmHg}$ . We also compared our system with commercial portable intraocular pressure (IOP) measurement devices, e.g., the Fa-800 Vet, FUAN [63] and the iCare IC 200 [64] with a respective measurement accuracy of  $\pm 1.5\ \text{mmHg}$  and  $\pm 1.2\ \text{mmHg}$  ( $\leq 20\ \text{mmHg}$ ). Our system demonstrates an even higher accuracy compared to commercial portable IOP measurement devices.

**Tracking the IOP Variations.** We explore Cyclops’s capability to continuously monitor human IOP, which exhibits diurnal fluctuations, typically being lowest in the morning upon waking up and gradually peaking around noon [65]. In our investigation, we utilize a syringe pump to systematically manipulate pressure applied to the tag. The pressure is incrementally increased from  $5\ \text{mmHg}$  to  $28\ \text{mmHg}$  and then continuously reduced back to  $5\ \text{mmHg}$ . This loading and unloading procedure is repeated for **24 hours**. To provide a benchmark, we also employ a stepwise pressure variation pattern. Here, we apply a specific pressure to the contact lens,

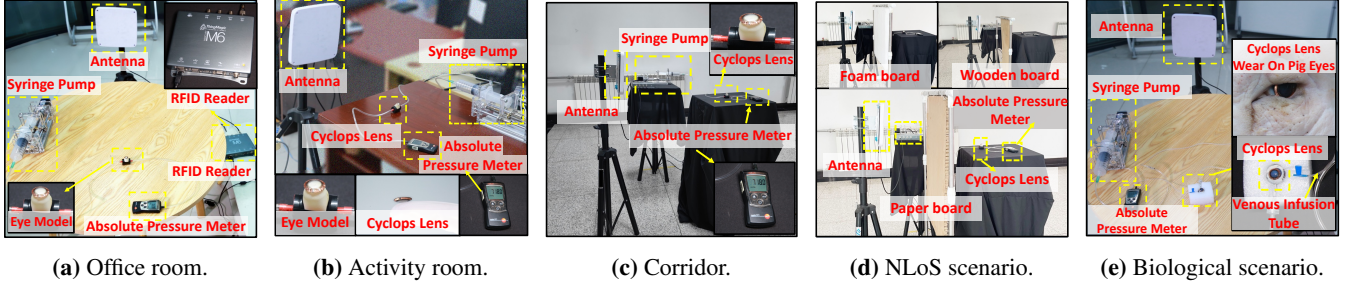


**Figure 20. The experiment settings.** To understand the impact of multipath, we conduct experiments inside the office, an activity room, and a corridor. To understand the NLoS, we block the LoS using various materials. We also conduct our experiments on pig eyes to investigate the biological impact.

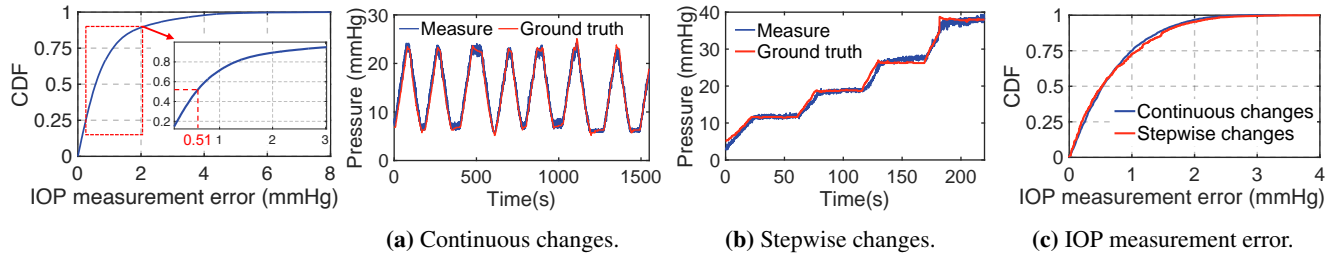


**Figure 21.** The estimation error for IOP measurement.

**Figure 22.** Performance on tracking the IOP variations. We conduct continuous and stepwise IOP measurement patterns and generate the cumulative distribution function of measurements.

maintain it for 30 seconds, and then gradually increase or decrease it to reach another specified pressure level. We also test the stepwise pattern for 24 hours to test Cyclops’s robustness.

The results depicted in Figure 22(a) and (b) showcase Cyclops’s remarkable IOP tracking performance under both continuous and stepwise patterns, exhibiting only minor deviations from the ground truth. Figure 22(c) illustrates the CDF of IOP estimation errors during the 24-hour test. The median IOP tracking errors for the continuous and stepwise patterns are 0.53 mmHg and 0.54 mmHg, respectively. These findings demonstrate Cyclops’s precision and robustness in IOP monitoring, particularly during prolonged tracking sessions, highlighting its potential in clinical applications where accurate and continuous IOP measurement is crucial.

**Impact of Environment and Distance.** We plot the cumulative distribution function of Cyclops’s IOP measurement error measured with different reader-chip distances in Figure 23 lower, and the median error of each distance in Figure 23 upper. We plot the results obtained from the office, the activity room, and the corridor in Figure 23(a), (b) and (c).

The median error in IOP measurements varies between [0.3, 0.75] mmHg, [0.35, 1.02] mmHg, and [0.37, 1.1] mmHg for the office, activity room, and corridor, respectively. Remarkably, there is no significant disparity in IOP measurement performance across these diverse testing environments, despite variations in their multipath profiles. This consistency arises from the inherent separation of the sensing and communication processes within our system. Sensing is primarily achieved through impedance matching, while the reader em-

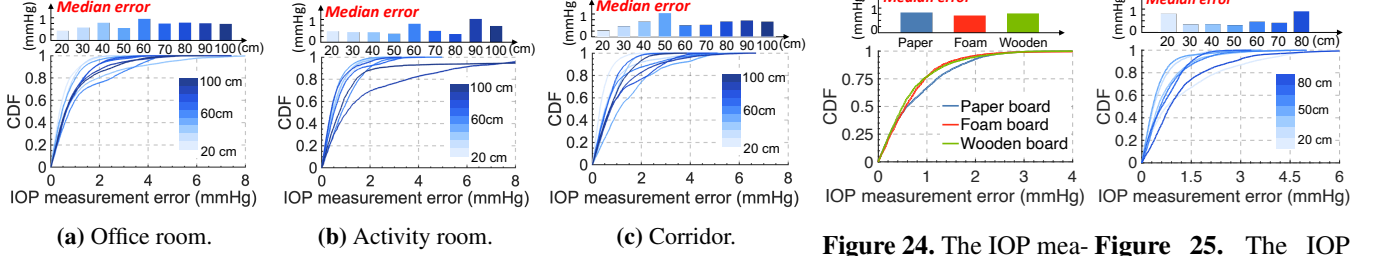
ploys backscatter communication to query the sensing data, specifically the 9-bit register value. In contrast to techniques that rely on analyzing the backscattered signal, such as phase variation calculations, our sensing quality remains largely independent of the received signal quality.

Nonetheless, it is worth noting that our sensing performance is influenced by signal quality to some extent, for example, the median error is smaller when the reader-chip distance is less than 50 centimeters, as shown in Figure 23. This improvement is attributed to enhance the accuracy of impedance matching when the received signal strength is substantially higher. Beyond this range, we do not see a clear trend between the reader-chip distance and the IOP measurement error, demonstrating the decoupling of sensing performance and the communication signal strength.

**Impact of NLoS.** We introduce various obstructing objects between the tag and the reader antenna to create NLoS scenarios, just as shown in Figure 20(d). The objects include a paper board, a foam board and a wooden board,. The distance between the antenna and the contact lens remains at 70 cm. We plot the IOP error in Figure 24. We see that the median errors are 0.562 mmHg, 0.589 mmHg, 0.505 mmHg, when the obstructing objects are a wooden board, a paper board, and a foam, respectively. This experiment further demonstrates that our sensing performance is decoupled with the signal quality.

### 6.3 Biological Impact on the Performance

We use pig eyes to assess the biological impact on our system’s performance, since the structure of pig eyes closely



(a) Office room.

(b) Activity room.

(c) Corridor.

**Figure 23.** The measurement error of IOP varies with the distance between the reader and the contact lens in three different environments.

**Figure 24.** The IOP measurement error in non-line-of-sight scenario. pig eyes.

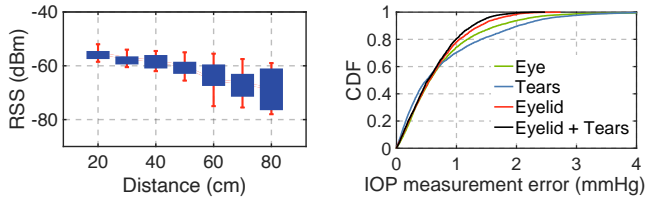


**Figure 26.** The measured RSS on pig eyes.

**Figure 27.** Impact of various biological tissues.

resembles that of human eyes, including intraocular pressure regulation and eye size. We examine Cyclops's performance in various bio-environments<sup>4</sup>, to explore the effects of different eye shapes, tear compositions, and the eyelid.

**End-to-end Performance on Pig Eyes.** To measure IOP on pig eyes, we put the contact lens on the eyes as shown in Figure 20(e). We use two venous infusion tubes to create two channels in the pig's eyes, as shown in Figure 20(e). One tube connects to a syringe pump for pressure control, and another connects to a pressure meter to obtain ground truth. The CDF of the estimation error is shown in the Figure 25. Even though the communication range slightly decreases to 80 cm, Cyclops still achieves high accuracy on pig eyes. The median error varies within the range of [0.33, 0.85] mmHg across distances, which is lower than that of commercial portable IOP measurement devices. The performance in the biological environment validates the efficacy of our approach.

**Impact of Eyeball Shapes.** Different individuals have varying eyeball shapes. To validate the robustness of our system across different organisms, we place the contact lens on ten different pig eyes and measure the RSS of the backscatter signal. The measurement results are shown in Figure 26. The communication distance ranges are similar for all 10 pig eyes, i.e., 80 cm. Despite the shape variations between pig eyes, the average RSS deviation remains around 3.29 dBm over distance. These results demonstrate that the performance of the Cyclops is consistent across pig eyes of different shapes.

**The Impact of Tears and Eyelids.** In order to make our user scenario closer to the real biological environment, we also investigate the impact of tears and eyelids. To evaluate the

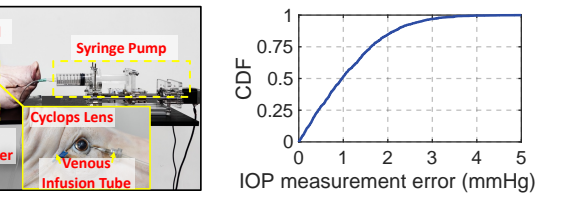
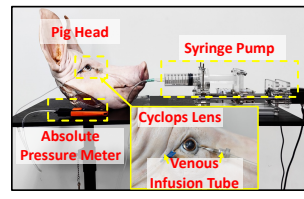
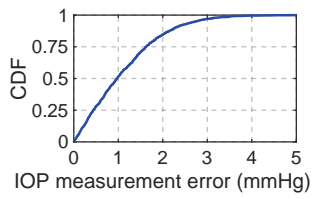


**Figure 25.** The IOP measurement error on line-of-sight scenario. pig eyes.



(a) Pig head.



(b) IOP measurement error.

**Figure 26.** IOP measurement performance on pig head.

effect of the tears, we drip around 0.05 mL of artificial tear fluid onto the pig eyes and measure the IOP under varying reader-chip distances. We also add eyelids on pig eyes and test its impact. We plot the IOP error measured from the contact lens worn on pure pig eyes, pig eyes with tears, pig eyes with eyelids and pig eyes with both eyelids and tears, in Figure 27, from which we see that the median error is 0.5 mmHg, 0.55 mmHg, 0.54 mmHg and 0.6 mmHg, respectively. With the pig eyelid and tears, we observe that our system achieves nearly the same performance as pure pig eyes, which meets the requirements of real-world IOP measurement.

**Performance Evaluation on Pig Head.** To evaluate the performance of our system more authentically, we attach the contact lens to the eyes of a pig. We attempt to change the IOP of the pig eyes by inserting a venous infusion tube from the edge of the eyes into the interior, as depicted in Figure 28(a). We also employed a pressure meter to monitor the real-time IOP changes in the pig eye. We display the cumulative distribution function of IOP measurement error from the contact lens under this scenario. As shown in Figure 28(b), the median error is 0.97 mmHg which still demonstrates good performance compared to commodity portable IOP measurement devices.

## 7 Conclusion

In this work, we introduce Cyclops, a wearable contact lens that can continuously measure intraocular pressure changes over a long distance. Through comprehensive introduction and experimental evaluation, we demonstrate the effectiveness of the system in measuring IOP changes in real-world settings and biological environments.

<sup>4</sup>With the approval of university's institutional review board (IRB).

## References

- [1] Jamie D Steinmetz, Rupert RA Bourne, Paul Svitil Briant, Seth R Flaxman, Hugh RB Taylor, Jost B Jonas, Amir Aberhe Abdoli, Woldu Aberhe Abrha, Ahmed Abualhasan, Eman Girum Abu-Gharbieh, et al. Causes of blindness and vision impairment in 2020 and trends over 30 years, and prevalence of avoidable blindness in relation to vision 2020: the right to sight: an analysis for the global burden of disease study. *The Lancet Global Health*, 9(2):e144–e160, 2021.
- [2] Yih-Chung Tham, Xiang Li, Tien Y Wong, Harry A Quigley, Tin Aung, and Ching-Yu Cheng. Global prevalence of glaucoma and projections of glaucoma burden through 2040: a systematic review and meta-analysis. *Ophthalmology*, 121(11):2081–2090, 2014.
- [3] Matthew J Burton, Jacqueline Ramke, Ana Patricia Marques, Rupert RA Bourne, Nathan Congdon, Iain Jones, Brandon AM Ah Tong, Simon Arunga, Damodar Bachani, Covadonga Bascaran, et al. The lancet global health commission on global eye health: vision beyond 2020. *The Lancet Global Health*, 9(4):e489–e551, 2021.
- [4] Joohee Kim, Jihun Park, Young-Geun Park, Eunkyung Cha, Minjae Ku, Hyeon Seok An, Kyoung-Pil Lee, Man-Il Huh, Junmo Kim, Taek-Soo Kim, et al. A soft and transparent contact lens for the wireless quantitative monitoring of intraocular pressure. *Nature Biomedical Engineering*, 5(7):772–782, 2021.
- [5] Kevin Gillmann, Robert N Weinreb, and Kaweh Mansouri. The effect of daily life activities on intraocular pressure related variations in open-angle glaucoma. *Scientific reports*, 11(1):6598, 2021.
- [6] Da Young Shin, Kyoung In Jung, Hae Young Lopilly Park, and Chan Kee Park. The effect of anxiety and depression on progression of glaucoma. *Scientific Reports*, 11(1):1769, 2021.
- [7] Guo-Zhen Chen, Ion-Seng Chan, Leo KK Leung, and David CC Lam. Soft wearable contact lens sensor for continuous intraocular pressure monitoring. *Medical engineering & physics*, 36(9):1134–1139, 2014.
- [8] Tae Yeon Kim, Jee Won Mok, Sang Hoon Hong, Sang Hoon Jeong, Hyunsik Choi, Sangbae Shin, Choun-Ki Joo, and Sei Kwang Hahn. Wireless theranostic smart contact lens for monitoring and control of intraocular pressure in glaucoma. *Nature Communications*, 13(1):6801, 2022.
- [9] Tae Yeon Kim, Sangbae Shin, Hyunsik Choi, Sang Hoon Jeong, David Myung, and Sei Kwang Hahn. Smart contact lenses with a transparent silver nanowire strain sensor for continuous intraocular pressure monitoring. *ACS Applied Bio Materials*, 4(5):4532–4541, 2021.
- [10] Yushi Zhang, Yufeng Chen, Tianxing Man, Dong Huang, Xiao Li, Hongwei Zhu, and Zhihong Li. High resolution non-invasive intraocular pressure monitoring by use of graphene woven fabrics on contact lens. *Microsystems & nanoengineering*, 5(1):1–8, 2019.
- [11] Yu Pang, Yuxing Li, Xuefeng Wang, Chenjie Qi, Yi Yang, and Tian-Ling Ren. A contact lens promising for non-invasive continuous intraocular pressure monitoring. *RSC advances*, 9(9):5076–5082, 2019.
- [12] Jiandong Xu, Tianrui Cui, Thomas Hirtz, Yancong Qiao, Xiaoshi Li, Fanhui Zhong, Xiaolin Han, Yi Yang, Sheng Zhang, and Tian-Ling Ren. Highly transparent and sensitive graphene sensors for continuous and non-invasive intraocular pressure monitoring. *ACS applied materials & interfaces*, 12(16):18375–18384, 2020.
- [13] Vladimir Laukhin, Irene Sánchez, Ana Moya, Elena Laukhina, Raul Martin, Fernando Ussa, Concepció Rovira, Anton Guimera, Rosa Villa, Jordi Aguiló, et al. Non-invasive intraocular pressure monitoring with a contact lens engineered with a nanostructured polymeric sensing film. *Sensors and Actuators A: Physical*, 170(1-2):36–43, 2011.
- [14] Matteo Leonardi, Peter Leuenberger, Daniel Bertrand, Arnaud Bertsch, and Philippe Renaud. First steps toward noninvasive intraocular pressure monitoring with a sensing contact lens. *Investigative ophthalmology & visual science*, 45(9):3113–3117, 2004.
- [15] Yanyan Fan, Hailing Tu, Hongbin Zhao, Feng Wei, Yi Yang, and Tianling Ren. A wearable contact lens sensor for noninvasive in-situ monitoring of intraocular pressure. *Nanotechnology*, 32(9):095106, 2020.
- [16] Guo-Zhen Chen, Ion-Seng Chan, and David CC Lam. Capacitive contact lens sensor for continuous non-invasive intraocular pressure monitoring. *Sensors and Actuators A: Physical*, 203:112–118, 2013.
- [17] Joohee Kim, Jaeyoon Kim, Minjae Ku, Eunkyung Cha, Seoyoung Ju, Won Yeong Park, Ki Hean Kim, Dai Woo Kim, Per-Olof Berggren, and Jang-Ung Park. Intraocular pressure monitoring following islet transplantation to the anterior chamber of the eye. *Nano letters*, 20(3):1517–1525, 2019.
- [18] Joohee Kim, Minji Kim, Mi-Sun Lee, Kukjoo Kim, Sangyoon Ji, Yun-Tae Kim, Jihun Park, Kyungmin Na, Kwai-Hyun Bae, Hong Kyun Kim, et al. Wearable smart sensor systems integrated on soft contact lenses for wireless ocular diagnostics. *Nature communications*, 8(1):1–8, 2017.
- [19] Cheng Yang, Qianni Wu, Junqing Liu, Jingshan Mo, Xiangling Li, Chengduan Yang, Ziqi Liu, Jingbo Yang, Lelun Jiang, Weirong Chen, et al. Intelligent wireless theranostic contact lens for electrical sensing and regulation of intraocular pressure. *Nature communications*, 13(1):1–15, 2022.
- [20] Jinyuan Zhang, Kyunghun Kim, Ho Joong Kim, Dawn Meyer, Woohyun Park, Seul Ah Lee, Yumin Dai, Bongjoong Kim, Haesoo Moon, Jay V Shah, et al. Smart soft contact lenses for continuous 24-hour monitoring of intraocular pressure in glaucoma care. *Nature communications*, 13(1):1–15, 2022.
- [21] M Hossein M Kouhani, Jiajia Wu, Arman Tavakoli, Arthur J Weber, and Wen Li. Wireless, passive strain sensor in a doughnut-shaped contact lens for continuous non-invasive self-monitoring of intraocular pressure. *Lab on a Chip*, 20(2):332–342, 2020.
- [22] Matteo Leonardi, Elie M Pitchon, Arnaud Bertsch, Philippe Renaud, and Andre Mermod. Wireless contact lens sensor for intraocular pressure monitoring: assessment on enucleated pig eyes. *Acta ophthalmologica*, 87(4):433–437, 2009.
- [23] Mohammad Hossein Mazaheri Kouhani, Arthur Weber, and Wen Li. Wireless intraocular pressure sensor using stretchable variable inductor. In *2017 IEEE 30th International Conference on Micro Electro Mechanical Systems (MEMS)*, pages 557–560. IEEE, 2017.
- [24] Chien-Kai Tseng, Yu-Chieh Huang, Shang-Wei Tsai, Guan-Ting Yeh, Chung-Hao Chang, and Jin-Chern Chiou. Design and fabricate a contact lens sensor with a micro-inductor embedded for intraocular pressure monitoring. In *SENSORS, 2012 IEEE*, pages 1–4. IEEE, 2012.
- [25] Martin Dressel and George Grüner. *Electrodynamics of solids: optical properties of electrons in matter*, 2002.
- [26] Anandghan Waghmare, Youssef Ben Taleb, Ishan Chatterjee, Arjun Narendra, and Shwetak Patel. Z-Ring: Single-Point Bio-Impedance Sensing for Gesture, Touch, Object and User Recognition. In *Proceedings of the 2023 CHI Conference on Human Factors in Computing Systems*, pages 1–18, 2023.
- [27] Wei Sun, Yuwen Chen, Yanjun Chen, Xiaopeng Zhang, Simon Zhan, Yixin Li, Jiecheng Wu, Teng Han, Haipeng Mi, Jingxian Wang, et al. MicroFluID: A Multi-Chip RFID Tag for Interaction Sensing Based on Microfluidic Switches. *Proceedings of the ACM on Interactive, Mobile, Wearable and Ubiquitous Technologies*, 6(3):1–23, 2022.
- [28] Goldmann applanation tonometry. [https://en.wikipedia.org/w/index.php?title=Goldmann\\_Applanation\\_Tonometer](https://en.wikipedia.org/wiki/Goldmann_Applanation_Tonometer).
- [29] Omar S Punjabi, Christoph Kniestedt, Robert L Stamper, and Shan C Lin. Dynamic contour tonometry: principle and use. *Clinical & experimental ophthalmology*, 34(9):837–840, 2006.
- [30] SY Hsu, MM Sheu, AH Hsu, KY Wu, JI Yeh, JN Tien, and RK Tsai. Comparisons of intraocular pressure measurements: Goldmann applanation tonometry, noncontact tonometry, tono-pen tonometry, and dynamic contour tonometry. *Eye*, 23(7):1582–1588, 2009.

- [31] Tanner J Ferguson, Catherine G Knier, Uttio Roy Chowdhury, Kjerset J Monson, Michael Greenwood, Russell J Swan, Richard Gorham, John P Berdahl, and Michael P Fautsch. Intraocular pressure measurement with pneumatonometry and a tonometer tip cover. *Ophthalmology and therapy*, 9:127–137, 2020.
- [32] Po-Jui Chen, Saloomeh Saati, Rohit Varma, Mark S Humayun, and Yu-Chong Tai. Implantable flexible-coiled wireless intraocular pressure sensor. In *2009 IEEE 22nd International Conference on Micro Electro Mechanical Systems*, pages 244–247. IEEE, 2009.
- [33] Jeong Oen Lee, Haeri Park, Juan Du, Ashwin Balakrishna, Oliver Chen, David Sretavan, and Hyuck Choo. A microscale optical implant for continuous in vivo monitoring of intraocular pressure. *Microsystems & nanoengineering*, 3(1):1–9, 2017.
- [34] Jeong Oen Lee, Vinayak Narasimhan, Juan Du, Blaise Ndjaméne, David Sretavan, and Hyuck Choo. Biocompatible multifunctional black-silicon for implantable intraocular sensor. *Advanced healthcare materials*, 6(4):1601356, 2017.
- [35] Amit Todani, Irmgard Behlau, Mark A Fava, Fabiano Cade, Daniel G Cherfan, Fouad R Zakka, Frederick A Jakobiec, Yuqing Gao, Claes H Dohlman, and Samii A Melki. Intraocular pressure measurement by radio wave telemetry. *Investigative ophthalmology & visual science*, 52(13):9573–9580, 2011.
- [36] Yuxuan Liu, Michael Zheng, Brendan O’Connor, Jingyan Dong, and Yong Zhu. Curvilinear soft electronics by micromolding of metal nanowires in capillaries. *Science Advances*, 8(46):eadd6996, 2022.
- [37] Jin-Chern Chiou, Yu-Chieh Huang, and Guan-Ting Yeh. A capacitor-based sensor and a contact lens sensing system for intraocular pressure monitoring. *Journal of Micromechanics and Microengineering*, 26(1):015001, 2015.
- [38] Ismail E Araci, Baolong Su, Stephen R Quake, and Yossi Mandel. An implantable microfluidic device for self-monitoring of intraocular pressure. *Nature medicine*, 20(9):1074–1078, 2014.
- [39] John Yan. An unpowered, wireless contact lens pressure sensor for point-of-care glaucoma diagnosis. In *2011 Annual International Conference of the IEEE Engineering in Medicine and Biology Society*, pages 2522–2525. IEEE, 2011.
- [40] Bohee Maeng, Hyung-kwan Chang, and Jungyul Park. Photonic crystal-based smart contact lens for continuous intraocular pressure monitoring. *Lab on a Chip*, 20(10):1740–1750, 2020.
- [41] Hongbin An, Liangzhou Chen, Xiaojun Liu, Bin Zhao, Hong Zhang, and Zhigang Wu. Microfluidic contact lenses for unpowered, continuous and non-invasive intraocular pressure monitoring. *Sensors and Actuators A: Physical*, 295:177–187, 2019.
- [42] Sevda Agaoglu, Priscilla Diep, Matthew Martini, KT Samudhyatha, Murat Baday, and I Emre Araci. Ultra-sensitive microfluidic wearable strain sensor for intraocular pressure monitoring. *Lab on a Chip*, 18(22):3471–3483, 2018.
- [43] Google lens. <https://blog.google/alphabet/introducing-your-smart-contact-lens/>.
- [44] Nicholas M Farandos, Ali K Yetisen, Michael J Monteiro, Christopher R Lowe, and Seok Hyun Yun. Contact lens sensors in ocular diagnostics. *Advanced healthcare materials*, 4(6):792–810, 2015.
- [45] Huanfen Yao, Angela J Shum, Melissa Cowan, Ilkka Lähdesmäki, and Babak A Parviz. A contact lens with embedded sensor for monitoring tear glucose level. *Biosensors and Bioelectronics*, 26(7):3290–3296, 2011.
- [46] Mojo. <https://www.mojo.vision/technology>.
- [47] Inwith. <https://inwithcorp.com/envisioning-reality/>.
- [48] Jihun Park, Joohee Kim, So-Yun Kim, Woon Hyung Cheong, Jiuk Jang, Young-Geun Park, Kyungmin Na, Yun-Tae Kim, Jun Hyuk Heo, Chang Young Lee, et al. Soft, smart contact lenses with integrations of wireless circuits, glucose sensors, and displays. *Science advances*, 4(1):eaap9841, 2018.
- [49] Andrew R Lingley, Muhammad Ali, Y Liao, Ramin Mirjalili, Maria Klonner, M Sopanen, Sami Suihkonen, Tueng Shen, Brian P Otis, H Lipsanen, et al. A single-pixel wireless contact lens display. *Journal of Micromechanics and Microengineering*, 21(12):125014, 2011.
- [50] Jagdish Pandey, Yu-Te Liao, Andrew Lingley, Ramin Mirjalili, Babak Parviz, and Brian P Otis. A fully integrated rf-powered contact lens with a single element display. *IEEE Transactions on Biomedical Circuits and Systems*, 4(6):454–461, 2010.
- [51] Do Hee Keum, Su-Kyoung Kim, Jahyun Koo, Geon-Hui Lee, Cheonhoo Jeon, Jee Won Mok, Beom Ho Mun, Keon Jae Lee, Ehsan Kamrani, Choun-Ki Joo, et al. Wireless smart contact lens for diabetic diagnosis and therapy. *Science advances*, 6(17):eaba3252, 2020.
- [52] Carolin Tetyczka, Kira Brisberger, Martin Reiser, Manuel Zettl, Ramona Jeitler, Christina Winter, Dagmar Kolb, Gerd Leitinger, Martin Spoerk, and Eva Roblegg. Itraconazole nanocrystals on hydrogel contact lenses via inkjet printing: implications for ophthalmic drug delivery. *ACS Applied Nano Materials*, 5(7):9435–9446, 2022.
- [53] Meysam Habibi, Saleh Mobasseri, Azam Zare, and Vahid Souriaee. Drug delivery with therapeutic lens for the glaucoma treatment in the anterior eye chamber: a numerical simulation. *Biomedical Engineering Advances*, 3:100032, 2022.
- [54] Woohyun Park, Van Phuc Nguyen, Yale Jeon, Bongjoong Kim, Yanxiu Li, Jonghun Yi, Hyungjun Kim, Jung Woo Leem, Young L Kim, Dong Rip Kim, et al. Biodegradable silicon nanoneedles for ocular drug delivery. *Science Advances*, 8(13):eabn1772, 2022.
- [55] Sijin Li, Andreea Pasc, Vanessa Fierro, and Alain Celzard. Hollow carbon spheres, synthesis and applications—a review. *Journal of Materials Chemistry A*, 4(33):12686–12713, 2016.
- [56] Zhiguang Qiu, Yongbiao Wan, Wohua Zhou, Jingyi Yang, Junlong Yang, Jun Huang, Jianming Zhang, Qingxian Liu, Siya Huang, and Ningning Bai. Ionic skin with biomimetic dielectric layer templated from calathea zebrina leaf. *Advanced Functional Materials*, 28(37):1802343.1–1802343.9, 2018.
- [57] Magnus s3. <https://www.axzon.com/packagedQFN.html>.
- [58] Jin-Woong Kim and Kyung-Do Suh. Monodisperse micron-sized polystyrene particles by seeded polymerization: effect of seed crosslinking on monomer swelling and particle morphology. *Polymer*, 41(16):6181–6188, 2000.
- [59] teato 510i. <https://www.testo.com/en-US/testo-510i/p/0560-1510>.
- [60] Hioki im7580. [https://www.hioki.com/global/products/lcr-meters/3-ghz/id\\_5913](https://www.hioki.com/global/products/lcr-meters/3-ghz/id_5913).
- [61] R&s znb8 vector network analyzer. [https://www.rohde-schwarz.com/us/products/test-and-measurement/network-analyzers/rs-znb-vector-network-analyzer\\_63493-11648.html](https://www.rohde-schwarz.com/us/products/test-and-measurement/network-analyzers/rs-znb-vector-network-analyzer_63493-11648.html).
- [62] Thingmagic mercury6 rfid reader. <https://www.barcodediscount.com/catalog/thingmagic/part-m6-na-poe.htm>.
- [63] Portable ophthalmic equipment. <https://sh-fuan.en.made-in-china.com/product/FQQtBMexCNYn/China-Portable-Ophthalmic-Equipment-Veterinary-Tonometer-Cat-Dog-Fa-800vet-Pet-Hospital-Animal-Tonometer.html>.
- [64] icare ic200. <https://www.icare-world.com/us/product/icare-ic200-tonometer/>.
- [65] Edward Hughes, Paul Spry, and Jeremy Diamond. 24-hour monitoring of intraocular pressure in glaucoma management: a retrospective review. *Journal of glaucoma*, 12(3):232–236, 2003.
- [66] Shubin Ma, Toni Björninen, Lauri Sydänheimo, Merja H Voutilainen, and Leena Ukkonen. Double split rings as extremely small and tuneable antennas for brain implantable wireless medical Microsystems. *IEEE Transactions on Antennas and Propagation*, 69(2):760–768, 2020.

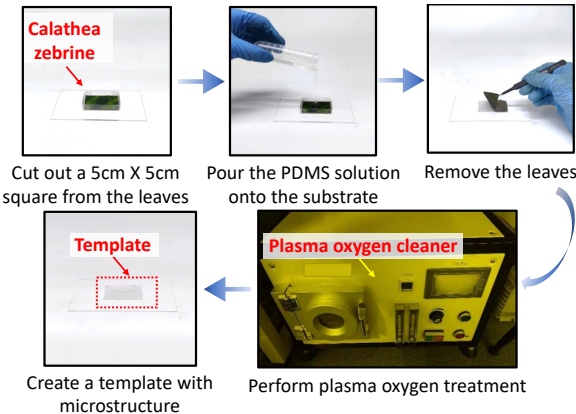


**Figure 29.** The template fabrication workflow.

## A Tag fabrication workflow

The manufacturing process of our tag mainly consists of three steps: synthesis of UHCS, *Calathea zebrae* mold casting, and tag production. The specific details are as follows:

### A.1 Calathea Zebrane Template.

**Step 1: Preparing Leaves.** Take the fresh *Calathea zebrae* leaves and cut them into suitable rectangular shapes ( $5\text{ cm} \times 5\text{ cm}$ ) from the center of the whole leaves, removing the leaf edges to ensure a consistent microstructure on the surface. Then washed them at least five times with deionized water to remove surface impurities. Afterward, place the leaves in a drying oven to remove surface moisture.

**Step 2: Casting the Template.** Multiple vent holes are manually created on the back of the prepared *Calathea zebrae* leaves, and the leaves are fixed with the front side up on a glass substrate. We prepared a PDMS solution by mixing PDMS base and curing agent in a ratio of 5:1 and poured onto the *Calathea zebrae* leaves. The assembly is placed in a vacuum chamber at  $20^\circ\text{C}$  until the bubbles disappear. After the bubbles disappear, the temperature is raised to  $80^\circ\text{C}$  for curing for two hours.

**Step 3: Plasma Oxygen Treatment.** After peeling off the *Calathea zebrae* leaves, we obtain a template with the sunken structure. Then we expose the formed template to air plasma treatment for one minute. This step involves a hydrophobic treatment process that prevents materials from sticking to the template. The sunken structure template can be reused multiple times.

### A.2 Synthesis of UHCS.

**Step 1: Synthesis the Polystyrene (PS) Nanoparticle.** We use the seeded swelling polymerization method to synthesize the polystyrene nanoparticle. Specifically, we added 20 g

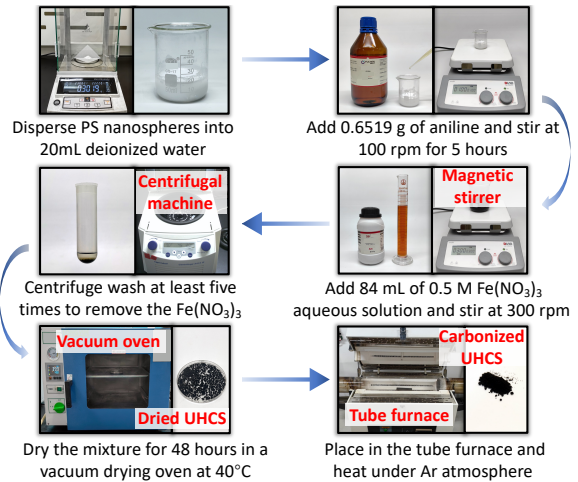


**Figure 30.** The UHCS synthesis workflow.

of styrene, 0.2 g of 2,2-azobisisobutyronitrile, and 1.8 g of polyvinyl pyrrolidone into a mixture of 60.4 g of ethanol and 7.6 g of deionized water. The mixture is then stirred under a nitrogen atmosphere at 900 rpm for one hour. Then heated to  $70^\circ\text{C}$  for 24 hours. After vacuum filtration and drying, we obtained the powdered PS nanoparticles.

**Step 2: Synthesis the PS Polyaniline Core-shell Spheres.** We take 0.3 g of the PS nanospheres and wash them using deionized for five times. Then, we disperse them into 20 mL of deionized water. Subsequently, we add 0.6519 g of aniline and stir it at 100 rpm for 5 hours to initiate the polymerization of aniline. Following this step, we add 84 mL of 0.5 M  $\text{Fe}(\text{NO}_3)_3$  aqueous solution into the reaction and stir it at 300 rpm for 24 hours at room temperature. The 0.5 M  $\text{Fe}(\text{NO}_3)_3$  can help to form the aniline spines on the PS surface.

**Step 3: Synthesis the UHCS.** During the last step, the PS polyaniline core-shell spheres are obtained. These spheres need to be washed at least five times to remove the  $\text{Fe}(\text{NO}_3)_3$ . Subsequently, the core-shell spheres are placed in a vacuum oven at  $40^\circ\text{C}$  for 48 hours to facilitate drying and remove any remaining moisture. Then, the core-shell spheres are placed into the tube furnace and heated at  $350^\circ\text{C}$  under an  $\text{Ar}$  atmosphere for one hour to eliminate the PS cores. In this step, we need to control the heating speed, gradually heating to  $350^\circ\text{C}$  at a rate of  $1^\circ\text{C}/\text{min}$ . If the temperature increase too fast, the gaseous PS cores will suddenly explode from inside the carbon sphere. The carbon sphere will break due to the explosion, just as shown in Figure 31. After removing the PS core, the temperature is then increased to  $900^\circ\text{C}$  at a rate of  $2^\circ\text{C}$  per minute for carbonization in order to obtain UHCS.

### A.3 UHCS-PDMS Film

Take 3 g of PDMS solution and 53.5 mg of UHCS powder, stir in a  $20^\circ\text{C}$  for one hour to mix them thoroughly. Then

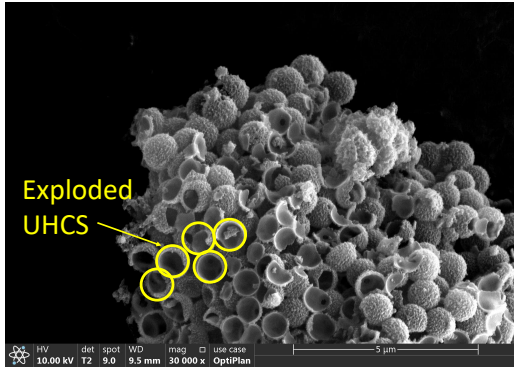


**Figure 31.** The scanning electron microscopy (SEM) image of the exploded UHCS.

pour the mixture onto the *Calathea zebrina* template and spin-coated the solution to obtain a UHCS-PDMS film with a thickness of  $60 \mu\text{m}$ . Next, heat it to  $80^\circ\text{C}$  for one hour to thermal curing. After peeling off the film from the template, the UHCS-PDMS film is formed with array of microcones.

We stack the top layer of the antenna and the UHCS-PDMS film with the bottom layer of the antenna. The chip is connected to the top layer of the antenna using the conductive silver paste. Then we coated the structure with the PDMS and heated at  $80^\circ\text{C}$  for 10 min, allowing the PDMS to partially solidify. While in this semi-solidified state, the PDMS is transferred to a contact lens mold for thermal curing at  $80^\circ\text{C}$  for one hour. Finally, we meticulously detach the cured antenna from the mold, remove the excess edges, and obtain the contact lens tag.

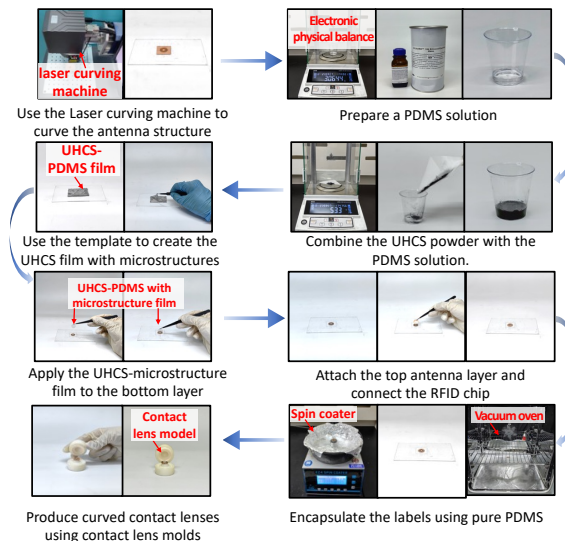


**Figure 32.** The Cyclops contact lens fabrication workflow.

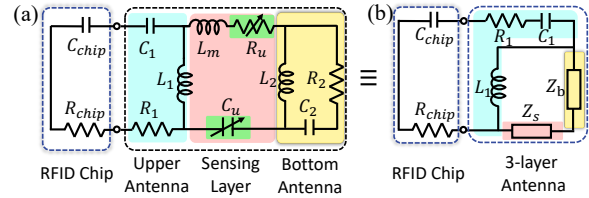


**Figure 33.** The equivalent circuit of the Cyclops lens antenna.

## B Impedance of the Cyclops lens Antenna

The equivalent circuit of the Cyclops lens antenna is shown in Figure 33(a). Where  $R_1$  and  $R_2$  denote the parasitic resistance of the upper layer and the bottom layer antenna.  $L_1$  and  $L_2$  represent parasitic capacitance, and  $C_1$  and  $C_2$  represent parasitic inductance of two antenna layers.  $L_m$  is the mutual-inductance between two antenna layers.  $C_u$  and  $R_u$  are variable capacitor and resistor, changing as the applied pressure varies.

From the equivalent circuit, we can observe that the  $C_1$ ,  $L_1$  and  $R_1$  are connected in series.  $L_m$  and  $R_u$  are in series and they are parallel connected with  $C_u$ . On the right side of the equivalent circuit,  $R_2$  and  $C_2$  are connected in series and the  $L_2$  is connected parallel to them. In order to simplify the entire circuit, we use  $Z_b$  to represent the impedance of the bottom layer, which can be represented as:

$$\begin{aligned} Z_b &= \left( -\frac{1}{j\omega C_2} + R_2 \right) // j\omega L_2 \\ &= \left( \frac{R_2 \cdot j\omega C_2 - 1}{j\omega C_2} \right) // j\omega L_2, \end{aligned} \quad (9)$$

where // represents the parallel relationship between the left-hand and right-hand sides of the formula. To calculate the total impedance of the bottom layer, we need to calculate the reciprocal of each individual branch impedance. Then we sum the reciprocals together. Finally, the total impedance of the parallel circuit  $Z_b$  is determined by taking the reciprocal of the resulting sum. The derivation process is as follows:

$$\begin{aligned} Z_b &= \frac{1}{\frac{j\omega C_2}{R_2 \cdot j\omega C_2 - 1} + \frac{1}{j\omega L_2}} \\ &= \frac{1}{\frac{j\omega C_2 \cdot j\omega L_2 + (R_2 \cdot j\omega C_2 - 1)}{(R_2 \cdot j\omega C_2 - 1)(j\omega L_2)}} \\ &= \frac{j^2 \omega^2 R_2 L_2 C_2 - j\omega L_2}{j^2 \omega^2 L_2 C_2 + j\omega R_2 C_2 - 1} \\ &= \frac{\omega^2 R_2 L_2 C_2 + j\omega L_2}{1 + \omega^2 C_2 L_2 - j\omega R_2 C_2}. \end{aligned} \quad (10)$$

As shown in Figure 33(b), we use  $Z_b$  to represent  $R_2$ ,  $L_2$  and  $C_2$  in the equivalent circuit. So the  $Z_b$  is connected in series with  $L_m$ ,  $R_u$  and  $C_u$ . Then we utilize  $Z_s$  to represent the impedance of the sensing layer, which can be expressed as follows:

$$Z_s = -\frac{1}{j\omega C_u} + R_u + j\omega L_m. \quad (11)$$

We substitute  $Z_s$  and  $Z_b$  into the circuit, resulting in an equiv-

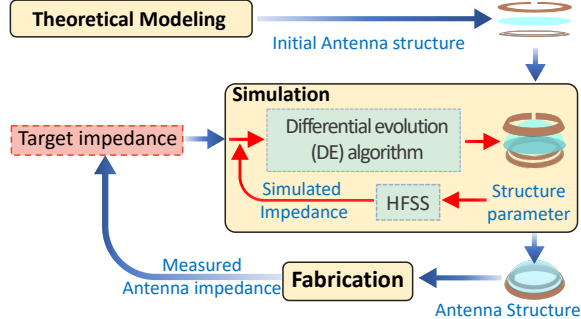


**Figure 34.** The workflow of fine-tuning the antenna impedance to match the target impedance.

alent circuit as shown in Figure 33(b).  $Z_s$  and  $Z_b$  are connected in series. Both of them are connected parallel with  $L_1$ . Then the parallel part is connected series with  $R_1$  and  $C_1$ . The impedance of the tag antenna can be represented as:

$$\begin{aligned}
 Z_{\text{ant}} &= -\frac{1}{j\omega C_1} + R_1 + j\omega L_1 / (Z_s + Z_b) \\
 &= -\frac{1}{j\omega C_1} + R_1 + \frac{1}{\frac{1}{j\omega L_1} + \frac{1}{Z_s + Z_b}} \\
 &= -\frac{1}{j\omega C_1} + R_1 + \frac{j\omega L_1 (Z_s + Z_b)}{j\omega L_1 + Z_s + Z_b}.
 \end{aligned} \tag{12}$$

## C Fine-Tuning Antenna Impedance

**Theoretical Modeling.** Considering the limited space of the human eyes, we first determine the basic ring shape for our antenna. Taking inspiration from inductively coupled loops [66], we design the antenna as a double rings with a split for con-

nnecting the RFID chip. Based on the basic antenna structure, we establish a theoretical model using microstrip transmission line theory. Then we estimate the antenna geometry by building an equivalent transmission line model. Calculate the transmission line resistance, inductance and capacitance based on the estimated antenna dimensions. Through conjugate impedance matching with the chip, we obtain the initial antenna structure just as shown in Fig.34.

**Simulation.** In practical implementation, our tag antenna requires curvature to fit the contours of the human eye. However, assessing the impact of this curving operation on the antenna's impedance is a challenge. Therefore, we rely on simulation software to replicate the effects of 3D curving and refine our design. We input the initial antenna structure into the simulation software to obtain a simulated antenna impedance. Subsequently, we employ the differential evolution algorithm to guide our parameter search process. After completing the simulation with a series of structure parameters, we obtain the simulated antenna impedance. This impedance data is subsequently utilized within our optimization algorithms, with the objective of achieving the target impedance.

**Iterative Fabrication and Simulation.** The final step involves fabricating the tag antenna based on the refined antenna structure and evaluate its actual impedance. Real-world manufacturing often introduces engineering errors leading to impedance deviations from the target value. To effectively minimize these deviations, we employ an iterative approach. We first update the simulation objective based on the difference between simulated and measured impedance values. This process iterates until we identify the antenna structure that optimally matches the target impedance, ensuring the best performance.